

# A model for magnetic flux leakage signal predictions

Catalin Mandache and Lynann Clapham

Department of Physics, Queen's University, Kingston, Ontario K7L 3N6, Canada

E-mail: mandache@physics.queensu.ca and lynann@physics.queensu.ca

Received 28 May 2003

Published 1 October 2003

Online at [stacks.iop.org/JPhysD/36/2427](http://stacks.iop.org/JPhysD/36/2427)

## Abstract

An analytical model was developed to determine the length of a surface-breaking defect along the direction of the applied field when using the magnetic flux leakage (MFL) non-destructive technique. The theoretical model fits the experimental MFL results from simulated defects. The extreme positions of the normal magnetic leakage field component were subsequently used for a quantitative evaluation of the defect length. Permeability variations were neglected by employing a flux density close to sample saturation. Four different defect geometries were experimentally investigated and the validity of the analytical model was verified. Good agreement between theoretical and experimental results suggests that this method can be used as an inverse MFL data interpretation technique.

## 1. Introduction

The ability to accurately assess the geometry of a surface-breaking defect in a ferromagnetic material through non-destructive testing is of critical importance for the oil and gas pipeline industry. One of the most popular inspection methods in this field is the magnetic flux leakage (MFL) technique. This consists of magnetizing the pipe in the axial direction and detecting defect-induced magnetic leakage fields using circumferentially arranged magnetic sensors. A corrosion pit in a background magnetic field acts as a region of high magnetic reluctance. Most of the flux lines are diverted around the defect, generating opposite magnetic polarities or a dipolar magnetic charge (DMC) on the defect walls.

Generally, defect geometry identification procedures are based on a direct (forward) approach. This scheme comprises of three steps: (1) conducting MFL runs on calibration samples and recording of MFL patterns of known defects; (2) *in situ* inspection of pipelines, and (3) analysis of results, with data from the field compared with MFL profiles generated by the calibration defects.

In this paper, we address a more useful and complex inverse method, aimed at eliminating the first step of the forward approach. In this inverse method the MFL signal of an initially unknown flaw is recorded and the defect geometry is estimated directly from the shape of the MFL profile.

Although quantitative correlation examples between the MFL signal amplitude and defect depth are abundant in the

literature, in general, the MFL relationship to defect length and width has been largely overlooked. Cracks and corrosion pits act as stress raisers in the pipe wall. The length and width of a flaw are very important for evaluating the local stress concentrations in the neighbourhood of a defect. The stress raiser factors are directly proportional to the length to width ratio of a defect [1]. Since oil and gas pipelines are operated at high pressures, the stress concentrations associated with defects can lead to pipeline failure.

In this paper, the defect 'length' is defined as its dimension along the applied field direction. Also, we refer to the magnetic leakage signal either as a 'flux' or a 'field'. Since the signal is measured in air, the MFL and magnetic leakage field are proportional, and the proportionality constant is  $\mu_0 = 4\pi \times 10^{-7} \text{ H m}^{-1}$ .

## 2. Background

Nearly all the theoretical studies published in the last three decades based on the interaction between magnetic fields and defects are based either on the theoretical development of Zatsepin and Shcherbinin [2] or Lord *et al's* finite element work [3, 4]. Hitherto, the difficulties associated with magnetic phenomena have limited the quantitative analysis of MFL signals to simple defect geometries.

Zatsepin and Shcherbinin [2] first approximated defects as point, line, and strip magnetic dipoles after proposing that the MFL signal arises from induced magnetic polarization at

the walls of a defect. Later on, Shcherbinin and Pashagin [5] improved this model by considering three-dimensional defects with rectangular cross-sections and parallel sides. Förster [6] analysed the same types of defects but accounted for the magnetic properties of the sample and the strength of the magnetizing fields. Edwards and Palmer [7] considered variations in the dipole strength with the magnetizing conditions of the sample. They showed that the relationships derived by Zatsepin and Shcherbinin [2] for infinitely long cracks (two-dimensional flaws) are valid also for finite cracks, provided the magnetic leakage field is examined along a line passing through the centre of the defect. Recently, Minkov *et al* [8,9] applied the dipolar model to single flaws of irregular cross-sections by considering the defect filled with magnetic dipoles aligned parallel to the magnetizing field, each individual dipole having a strength directly proportional to the defect depth. Therefore, this method essentially represents a discretization of the irregular cross-section defect in terms of individual strip dipoles.

To date, all published research based on the analytical model of DMC [2, 5–7, 10], with one exception [11], refers to a single defect. The often encountered practical situation of two adjacent defects is discussed only by Uetake and Saito [11], but their study is limited to slots with parallel walls, of a maximum of 4 mm in length. In this study we consider a multiple defect case. We define ‘interacting defects’ to be two neighbouring corrosion pits, with the axis joining their centres aligned with the direction of the applied field.

With increase in computational capabilities, finite element analysis can now compete with analytical methods. Since the pioneering numerical modelling of MFL phenomena by Lord and co-workers [3, 4, 12], the finite element analysis of defect-induced magnetic signals has become increasingly popular. In spite of the significant progress made in this area to include non-linear material properties and their anisotropy [13–15], a quantitative relationship between magnetic leakage field and defect length has not been clearly specified. Furthermore, numerical modelling involves a direct MFL approach, since it includes predefined defect geometries and material characteristics.

Calibration of the MFL signals in terms of defect depth has been studied both through finite element modelling [4, 12, 13, 15] and through analytical methods based on DMC [7, 12, 16]. Two of the numerical analysis studies [4, 15] correctly predicted that the amplitude of the normal MFL signal component increases with defect depth, and that the separation between the extreme MFL values is directly proportional to the defect length.

In this paper, we refine the DMC method [2, 5, 7] and adapt it for single and multiple circular defects. Four types of corrosion flaws are analysed: a single cylindrical hole, two adjacent interacting hole geometries, and a racetrack (elongated) defect. The results of the analytical model are compared with the experimental MFL profiles.

### 3. Formulation of the analytical model

Similar to the previous research of Edwards and Palmer [7], Shcherbinin and Pashagin [5] we assume that a DMC is developed on the defect faces intersecting the magnetic field,

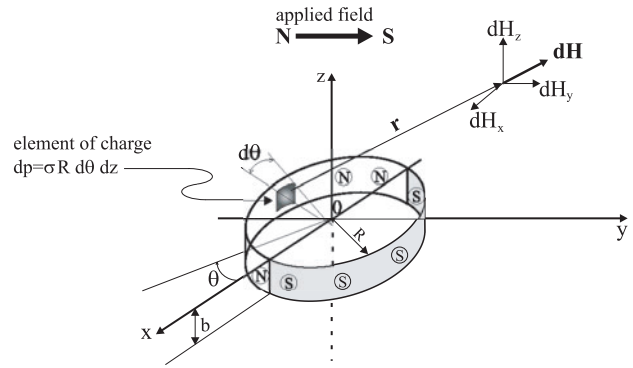


**Figure 1.** Dipolar representation of a cylindrical hole defect of radius  $R$ .

as a result of magnetic field—defect interaction. The DMC generates its own field and the problem becomes analogous to a uniform electric charge distribution.

In general, the modelling of the magnetic phenomena involved in non-destructive testing is complicated by the non-linearity of the material characteristics. In this study, local variations in magnetization and permeability were avoided by assuming high magnetic fields, corresponding to the saturation region of the sample.

Initially, a cylindrical single hole defect was considered, with its axis ( $z$ -direction) perpendicular to the applied magnetic field ( $y$ -direction), as schematically represented in figure 1. The defect was assumed to be air-filled and embedded in a ferromagnetic medium. The magnetic field lines diverge around the low permeability flaw, inducing a DMC on the walls of the cylinder, as shown in figure 1. The surface of the test piece is defined by the  $xy$  plane at  $z = 0$ , with the top area of the cylindrical defect centred at  $(0, 0, 0)$ , and its bottom area centred at  $(0, 0, -b)$ , where  $b$  represents the defect depth. The MFL signal induced by the type of defect just described was sampled in the region  $z > 0$ .

Opposite magnetic polarities appear on the walls of the cylinder. Because the defect is small in comparison to the region of the sample under the action of a uniform magnetic field this ‘charge’ was assumed to be distributed homogeneously on the surface of the hole.

As shown in figure 1, half of this cylinder develops a north polarity or positive magnetic charge density,  $+\sigma$ , while the other half has a south polarity or negative magnetic charge density,  $-\sigma$ . The cylindrical defect has a radius  $R$  and depth  $b$ . The angle  $\theta$  is measured from the positive  $x$ -direction to an element of magnetic charge,  $dp$ . The differential element of charge,  $dp$ , has coordinates  $(R \cos \theta, R \sin \theta, z)$  and a charge proportional to its area:

$$dp = \sigma R d\theta dz \quad (1)$$

The magnetic field ( $d\vec{H}$ ) generated at a distance  $\vec{r}$  by this element of charge ( $dp$ ) is given by [5, 7]

$$d\vec{H} = \frac{dp}{4\pi r^3} \cdot \vec{r} \quad (2)$$

Since the interest is only in finding the location of the extreme values of the magnetic leakage field, and not the MFL amplitude, the charge density,  $\sigma$ , is assigned a value of 1. The

$z$ -coordinate of the observation point represents the lift-off of the detection Hall probe,  $h$ , and it is always a positive constant.

Initially, only the positive polarity side of the hole (with  $y < 0$ , as shown in figure 1) and  $\theta$  measured from the positive  $x$ -axis in a clockwise direction is considered. The distance  $r_+$  from the charge  $d\rho$  to any point situated above the top surface of the specimen is

$$r_+ = [R^2 \cos^2 \theta + (y + R \sin \theta)^2 + (h - z)^2]^{1/2} \quad (3)$$

Combining equations (1)–(3), the components of the field at a distance  $r_+$  away are given by

$$dH_z^+ = \frac{R d\theta dz}{4\pi r_+^3} (h - z) \quad (4)$$

$$dH_y^+ = \frac{R d\theta dz}{4\pi r_+^3} (y + R \sin \theta) \quad (5)$$

The  $x$ -component of the leakage field,  $d\vec{H}_x^+$ , vanishes due to symmetry. Furthermore, since only the normal MFL ( $z$ -axis) component along the  $x = 0$  mm line was considered in the experimental study,  $x = 0$  was substituted into equations (3) and (4).

A double integration of equation (4) was applied over  $\theta$  from 0 to  $\pi$  and over  $z$  from  $-b$  ( $b > 0$ ) to 0 to determine the total field at  $r_+$  due to the positively polarized side of the defect:

$$H_z^+ = \frac{R}{4\pi} \int_0^\pi d\theta \times \int_{-b}^0 \frac{dz(h - z)}{[R^2 \cos^2 \theta + (y + R \sin \theta)^2 + (h - z)^2]^{3/2}} \quad (6)$$

The same approach is used for the negatively polarized side of the cylinder. The integral limits remain the same if we assume that the angle  $\theta$  is again measured from the positive  $x$ -axis, but now in a counter clockwise direction. The only changes in equations (4) and (6) have to take into account the opposite polarity (negative DMC) and an appropriate  $y$ -coordinate change:

$$y + R \sin \theta \rightarrow y - R \sin \theta \quad (7)$$

Therefore, the  $z$ -component of the magnetic leakage field generated by the negatively polarized side of the defect can be expressed as

$$H_z^- = -\frac{R}{4\pi} \int_0^\pi d\theta \times \int_{-b}^0 \frac{dz(h - z)}{[R^2 \cos^2 \theta + (y - R \sin \theta)^2 + (h - z)^2]^{3/2}} \quad (8)$$

The total normal leakage field along the  $x = 0$  profile is given by

$$H_z = H_z^+ + H_z^- \quad (9)$$

The solutions of the double integration of equations (6) and (8) were obtained using Maple 8, a symbolic computation software product [17], but are too lengthy to be included here.

The solutions for interacting and racetrack defects follow the same procedure as a single cylindrical defect situation discussed earlier. Note that after the integration of equations (6) and (8), we obtained functions depending

only on the  $y$  variable. For the case of two interacting holes, with one hole centred at  $(0, y + m, 0)$ , and the other centred at  $(0, y - n, 0)$ , appropriate substitutions have to be performed to obtain the total normal field component for this geometry:

$$H_z^{\text{total}} = H_z(y \rightarrow y + m) + H_z(y \rightarrow y - n) \quad (10)$$

The calculated results for the single, interacting, and racetrack geometries are considered in section 5. Because, in this study, we are not concerned with the amplitude of the magnetic signals and we assume a constant applied flux density, both the experimental and analytical results are normalized to their respective maximum absolute values.

#### 4. Experimental details

Four mild steel plate samples, each containing a defect of the type described in table 1 were investigated using the MFL method. All defects completely penetrate the steel plate; therefore, their depth is equal to the sample thickness. The defects were drilled by electrochemical milling. This procedure not only simulates a practically encountered corrosion mechanism, but also avoids introduction of additional stresses during the drilling process, as in the case in mechanical machining [18].

The ‘interacting-A’ defects were two similar circular holes with a centre-to-centre distance that was four times the radius of an individual hole. For the ‘interacting-B’ geometry the same arrangement is present, except the centre-to-centre distance was equal to three times the radius of a single hole. The racetrack defect was an elongated pit with the same end-to-end dimensions as the interacting—A geometry, but with the area between the holes milled away to create the shape of a racetrack.

The schematic of the MFL experimental arrangement is described elsewhere [18]. The magnetic flux applied to the mild steel test pieces was generated by a rare earth (NdFeB) permanent magnet. Local permeability variations were minimized by the application of a high magnetic flux density ( $\sim 1.6$  T). The magnetic induction corresponding to the saturation magnetization for mild steel is around 1.8–1.9 T.

A Hall probe (model SS94A1, manufactured by Honeywell) of active area  $1 \text{ mm}^2$  was used to scan the surface of the sample for the normal component of the leakage field. The Hall sensor moved with an incremental step of 1 mm on each direction on the specimen surface and scanned an area of  $80 \text{ mm} \times 80 \text{ mm}$  centred on the defect geometry. Due to the physical dimensions of the magnetic sensor and its

**Table 1.** Description of the defects analysed. In the case of (identical) interacting defects, only the length of one of the holes is included. For the racetrack defect the ‘radius’ represents the radius of curvature of the two rounded edges.

Defect	Depth (mm)	Radius (mm)	Length (mm)
Single hole	3.0	8	16
Interacting-A holes	2.8	9	18
Interacting-B holes	2.8	9	18
Racetrack	2.8	9	54

holder, a constant lift-off of 1.5 mm was maintained for all measurements. The MFL profile of the area scan cutting through the centres of the defects and aligned along the applied magnetic flux direction is analysed in the following section.

### 5. Results and discussion

The normal component MFL profiles for all four flaw geometries are shown in figures 2–5, where the inserted glyphs are schematic diagrams of the defects. Both the experimental and theoretical data are normalized with respect to their corresponding maximum amplitudes for comparison purposes. Normalization of the MFL values did not change the position of maximum amplitude points. The mathematical model was applied to the four experimental defect situations described in table 1. The constant lift-off of the Hall sensor ( $h = 1.5$  mm) is used as an input parameter of the analytical model.

In figure 2, the theoretical curve for a single defect was the result of the magnetic field obtained from equation (9). As seen, the agreement between the mathematical and experimental results is very good. Figures 3 and 4 show the

theoretical and experimental results for interacting-A (figure 3) and interacting-B (figure 4) defects, respectively. For these two cases, the theoretical model was adjusted to account for the effects of ‘flux shielding’ between defects, since closely spaced adjacent pits will shield the region between them from the applied field. The flux density is lower in this area than in the background region away from the defects. This effect is reflected in the lower charge density on the inside defect faces (the semi-cylindrical wall of the defect facing the other). In the model, the flux shielding effect is accounted for by assigning a lower DMC to the inside faces of the adjacent defects. For the case of interacting-A holes (figure 3), the theoretical curve was obtained by assigning a charge density of  $\sigma = 0.65$  to the inside walls ( $\sigma = 1.0$  on the outside walls). For the interacting-B holes (figure 4)  $\sigma = 0.40$  was used for the inside wall charge density. These charge density values were selected to best fit the experimental data for locations 2 and 3 of the MFL profiles shown in figures 3 and 4.

Finally, figure 5 shows the theoretical and experimental curves for the racetrack defect. In this case, the mathematical data was obtained in a manner similar to that for the

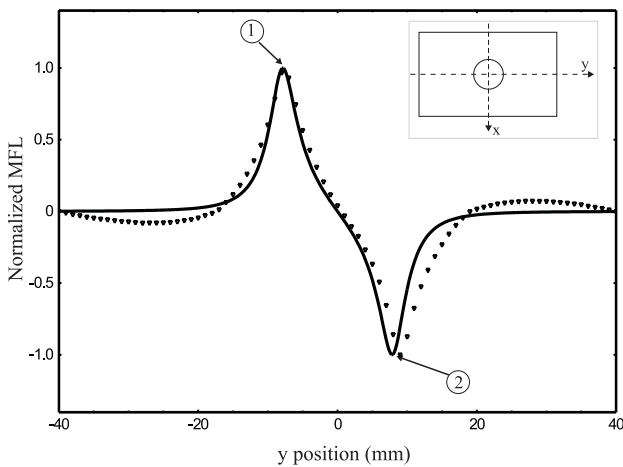


**Figure 2.** Theoretical (—) and experimental ( $\nabla$ ) normalized MFL for a single circular defect of radius  $R = 8$  mm. Results show the MFL line scan along the  $y$ -axis, at  $x = 0$ .

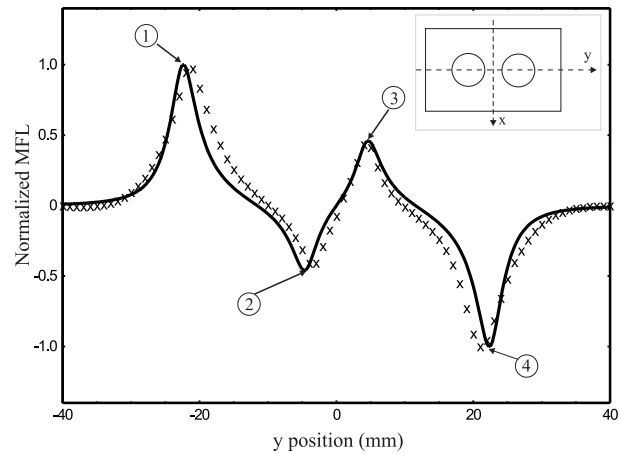


**Figure 4.** Theoretical (—) and experimental ( $\times$ ) normalized MFL for interacting-B defects. Radius of a defect  $R = 9$  mm. Results show the MFL line scan along the  $y$ -axis, at  $x = 0$ .

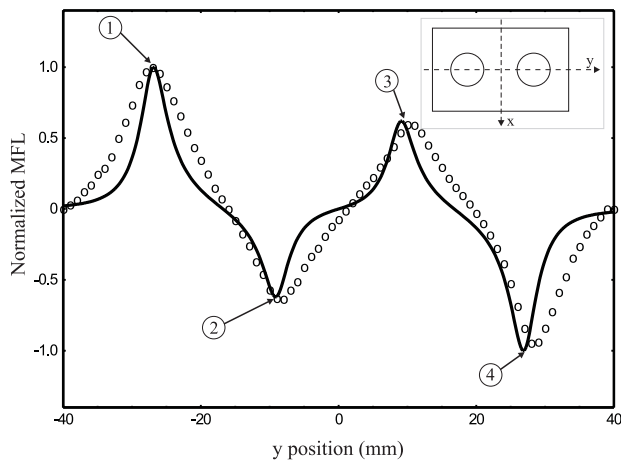


**Figure 3.** Theoretical (—) and experimental ( $\circ$ ) normalized MFL for interacting-A defects radius of a defect  $R = 9$  mm. Results show the MFL line scan along the  $y$ -axis, at  $x = 0$ .

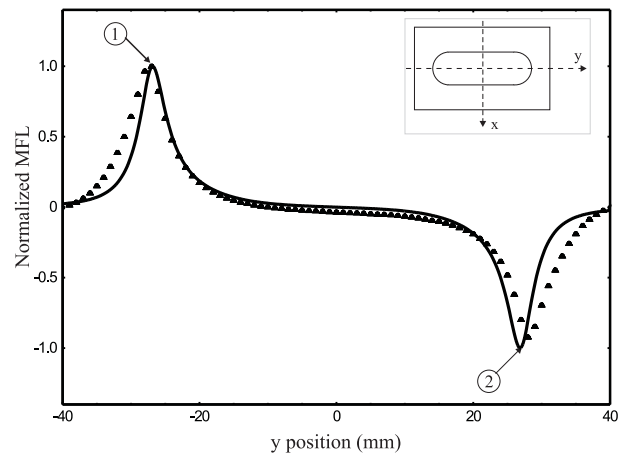


**Figure 5.** Theoretical (—) and experimental ( $\blacktriangle$ ) normalized MFL for a racetrack defect. Radius of curvature of the rounded edges:  $R = 9$  mm. Results show the MFL line scan along the  $y$ -axis, at  $x = 0$ .

**Table 2.** Defect lengths: actual measurement, as well as distances determined from experimental and theoretical MFL profiles (all dimensions are given in mm).

Method of measurement	Single hole	Interacting-A defects			Interacting-B defects			Racetrack
		Left hole	Right hole	Overall length	Left hole	Right hole	Overall length	
Actual measurement	16.0	18.0	18.0	54.0	18.0	18.0	45.0	54.0
Experimental MFL	17.0	19.0	18.0	55.0	18.0	17.0	43.0	55.0
Theoretical MFL	15.7	17.8	17.8	53.6	17.8	17.8	44.6	53.8

interacting-A defects, except that the charge density on the inside faces was set to  $\sigma = 0$ . Again, the agreement with experiment is very good.

The defect lengths obtained through actual measurements, plus their estimation from the mathematical and experimental results are given in table 2. The length of the single hole or racetrack defect was measured as the separation between the MFL values situated at the extremes 1 and 2 (see figures 2 and 5). For the interacting defects, the length of the left hole is the  $y$ -axis distance between 1 and 2, while the length of the right hole is the  $y$ -axis separation between positions 3 and 4. Also, the overall length of the interacting defects can be predicted from the distance between the MFL extreme values situated at positions 1 and 4 (figures 3 and 4).

Generally, the results obtained through both experimental and analytical methods give quite accurate estimations of the defect lengths for all four defect geometries. Selection of lower charge densities on the inside walls of the interacting defects emphasizes the special feature of the adjacent defects: they partially shield the area between them from the background magnetic field. The experimental results could be further improved if a smaller incremental step of MFL measurements and sensor lift-off were assured. Also, by implementing a lift-off parameter  $h \rightarrow 0_+$  in the theoretical model, the exact defect sizes could be obtained.

From a theoretical point of view, the model could be applied to other defect shapes and cross-sections by taking into account an appropriate variation of the DMC with flux shielding and depth. Stress effects could also be incorporated since they affect the magnetoelastic energy of the system, modify the easy axis direction and, as a consequence, change the intensity of the DMC represented by the defects [10].

## 6. Summary and conclusions

In this study, we have discussed the inverse problem of defect size prediction directly from MFL signals. An analytical model was modified to account for circular defects in order to correlate the normal component MFL profile with the defect dimension along the magnetic field orientation. The validity of the model was confirmed through comparison with experimental MFL scans from different defect geometries.

The theoretical model developed for a single cylindrical defect was adapted to more complex and realistic defect geometries, specifically, to interacting and racetrack defects. The phenomenon of magnetic flux shielding of the region

between two interacting defects was accounted for by lowering the magnitude of the magnetic charge on the inside walls of each interacting defect. Very good agreement between the mathematical results and experimental data was found for all defect geometries investigated.

A clear advantage of the method presented here is the low number of parameters that have to be considered when determining the length of defects using normal MFL profiles. The knowledge of material characteristics, such as permeability and coercivity are not necessary, as long as the inspection magnetic field strength corresponds to the saturation magnetization level of the sample.

## Acknowledgments

This work was supported by the Gas Technology Institute, Natural Sciences and Engineering Research Council of Canada, and Pipeline Integrity International.

## References

- [1] Juvinall R C 1967 *Engineering Considerations of Stress, Strain, and Strength* (New York: McGraw-Hill) chapter 13
- [2] Dobmann G and Höller P 1980 *Research Techniques in Nondestructive Testing* ed R S Sharpe (New York: Academic) vol IV, 39–69
- [3] Hwang J H and Lord W 1975 *J. Testing Eval.* **3** 21–5
- [4] Lord W and Hwang J H 1977 *Br. J. Non-destruct. Testing* **19** 14–18
- [5] Shcherbinin V E and Pashagin A I 1972 *Defektoskopiya* **8** 74–82
- [6] Förster F 1986 *NDT Int.* **19** 3–13
- [7] Edwards C and Palmer S B 1986 *J. Phys. D: Appl. Phys.* **19** 657–73
- [8] Minkov D, Takeda Y, Shoji T and Lee J 2002 *Appl. Phys. A* **74** 169–76
- [9] Minkov D, Lee J and Shoji T 2000 *J. Magn. Magn. Mater.* **217** 207–15
- [10] Mandal K and Atherton D L 1998 *J. Phys. D: Appl. Phys.* **31** 3211–17
- [11] Uetake I and Saito T 1997 *NDT & E Int.* **30** 371–7
- [12] Lord W, Bridges J M, Yen W and Palanisamy R 1978 *Mater. Eval.* **36** 46–54
- [13] Atherton D L and Daly M G 1987 *NDT Int.* **20** 235–8
- [14] Patel U and Rodger D 1995 *IEEE Trans. Magn.* **31** 2170–3
- [15] Altschuler E and Pignotti A 1995 *NDT & E Int.* **28** 35–40
- [16] Philip J, Rao C B, Jayakumar T and Raj B 2000 *NDT & E Int.* **33** 289–95
- [17] www.maplesoft.com 2002 *Maple 8.00* Waterloo Maple Inc., Waterloo, Canada
- [18] Plotnikov A and Clapham L 2002 *Insight* **44** 74–8